Chapter 2
Stretchability, Conformability, and Low-Cost Manufacture of Epidermal Sensors

Nanshu Lu, Shixuan Yang and Liu Wang

Abstract Epidermal sensors and electronics represent a class of artificial devices whose thickness, mass density, and mechanical stiffness are well-matched with human epidermis. They can be applied as temporary transfer tattoos on the surface of any part of human body for physiological measurements, electrical or thermal stimulation, as well as wireless communications. Except for comfort and wearability, epidermal sensors can offer unprecedented signal quality even under severe skin deformation. This chapter tries to address two fundamental mechanics challenges for epidermal sensors: first, how to predict and improve the stretchability and compliance when epidermal devices are made out of intrinsically brittle and rigid inorganic electronic materials; and second, when laminating on human skin, how to predict and improve the conformability between epidermal devices and the microscopically rough skin surfaces. Since the ideal use of epidermal devices would be one-time, disposable patches, a low cost, high throughput manufacture process called the "cut-and-paste" method is introduced at the end of this chapter.

Keywords Epidermal sensors · Stretchable · Serpentine · Conformability · Low-cost manufacture

2.1 Introduction

Development of high-performance wearable vital sign monitors is the central focus for the emerging field of mobile health (mHealth), one of the highest anticipated markets based on the Internet of Things (IoT) concept. High-fidelity sensing holds

N. Lu (✉) · S. Yang · L. Wang
Department of Aerospace Engineering and Engineering Mechanics,
Center for Mechanics of Solids, Structures, and Materials,
University of Texas at Austin, Austin, USA
e-mail: nanshulu@utexas.edu

N. Lu
Department of Biomedical Engineering, University of Texas at Austin, Austin, USA

J.A. Rogers et al. (eds.), *Stretchable Bioelectronics for Medical Devices and Systems*, Microsystems and Nanosystems,
DOI 10.1007/978-3-319-28694-5_2

the key to the success of wearable health monitors, which essentially demands both high signal-to-noise ratio and low susceptibility to motion artifacts. While wafer based sensors, electronics, optics, and conventional power sources exhibit high performance and superior chemical stability, their hard, planar, and rigid form factors are not compatible with the soft, curvilinear, and dynamic human body [1–3]. As a result, state-of-the-art wearable devices such as the wrist or arm bands and chest straps are not capable of intimate-skin integration and hence cannot provide medical-grade data.

Epidermal sensors and electronics represent a class of artificial devices that is fundamentally different from current wearable devices in terms of the form factor, wearability, and signal quality [4]. Through mechanics optimization [5–7] and innovation in materials processing [2, 8], stiff and brittle inorganic electronic materials can now be made soft and stretchable, which enabled tattoo-like patches with the thickness, mass density, and mechanical stiffness well matched with human epidermis, as demonstrated in Fig. 2.1a [4]. The key is to pattern intrinsically stiff and blanket high-performance nanomembranes into structurally soft and stretchable filamentary serpentines, and transfer print them from rigid wafers to ultrathin (e.g., 30 μm thick), skin-like elastomeric substrates, as shown in Fig. 2.1b left frame [4]. Although the device is made of intrinsically stiff gold (Au) and silicon (Si) nanomembranes with modulus in the 100 GPa regime, the overall mechanical stiffness of this epidermal sensor is measured to be 150 kPa, which is literally as soft as epidermis (160 kPa) [4]. Since serpentine is the enabling geometry for skin-soft sensors and electronics, the fundamental mechanics that predicts and optimizes the stretchability and compliance of serpentine is going to be the first topic of this chapter.

Due to the ultimate thinness and softness of epidermal sensors, laminating them on microscopically rough skin surface leads to fully conformal contact, as evidenced in Fig. 2.1b right frame [9]. Such conformal contact enhances contact area, which results in reduced skin-electrode interface impedance and improved sensor-skin adhesion. As a result, when skin deforms, even by van der Waals adhesion alone, the epidermal sensor is able to follow all kinds of skin distortion without any delamination, sliding, or imposing any mechanical constraint to the skin, essentially behaving like a secondary skin. Hence the second topic of this chapter will reveal the key parameters that govern the conformability between the device patch and the corrugated skin surface.

The suppressed interfacial sliding leads to the most distinctive advantage of epidermal sensors—the immunity from motion artifacts. Motion-induced noise and signal degradation is a ubiquitous problem in conventional health monitors, such as the long term, dry, capacitive electrocardiogram (ECG) electrodes [10]. Figure 2.1c [11] shows a direct comparison of ECGs simultaneously measured by conventional capacitive flat electrodes (upper frame) and epidermal electrodes (lower frame) from the same human subject. When the subject moved his upper body, motion artifacts were clearly present in the upper frame (as indicated by the red arrow), whereas the

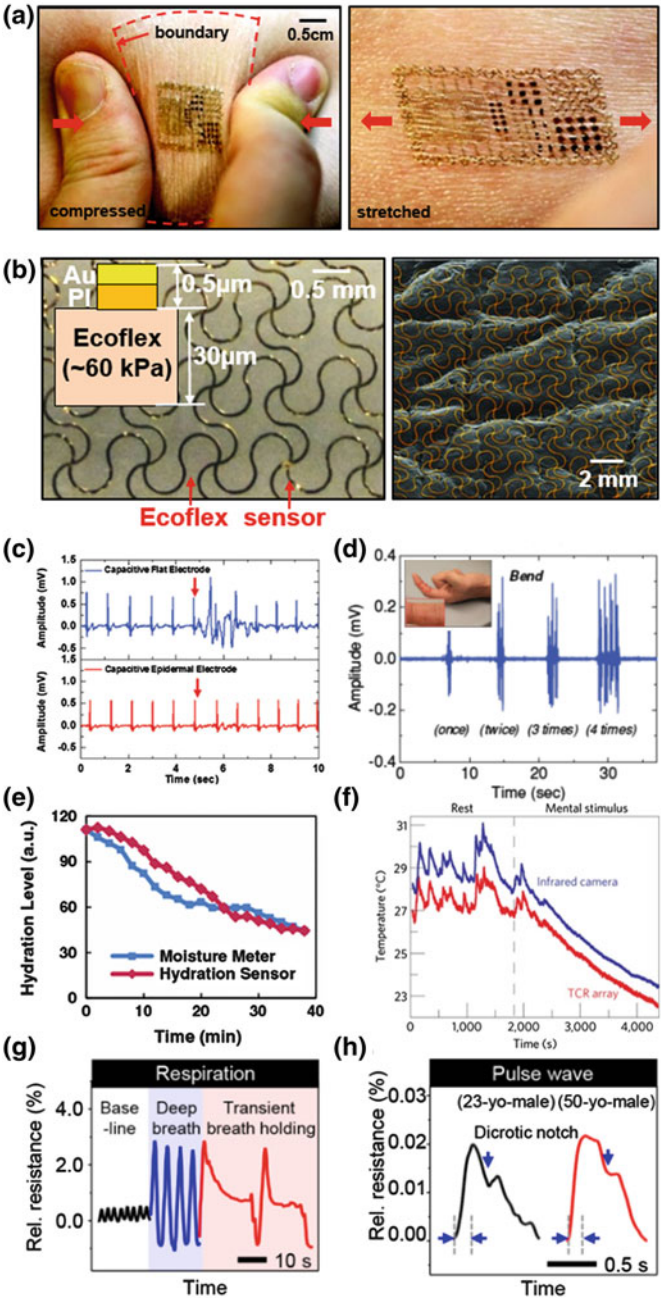

Fig. 2.1 Examples of epidermal sensors. **a** The first epidermal electronics [4]. **b** Filamentary serpentine design of gold electrodes showing extraordinary conformability on rough skin replica [9]. **c** Conventional dry ECG electrode is susceptible to motion artifacts (upper frame), whereas epidermal ECG sensor (bottom frame) is not affected at all [11]. **d** Epidermal EMG sensor measuring finger bend [12]. **e** Epidermal hydration sensor [13]. **f** Epidermal temperature detector [16]. **g** Epidermal strain gauge sensing respiration on the chest [17]. **h** Epidermal pulse wave sensor on the wrist [17]

signal acquired by the epidermal electrodes was not affected at all. For similar reasons, the electromyogram (EMG) measured from severe finger bend demonstrates extraordinary signal-to-noise ratio (Fig. 2.1d [12]). Not only electrophysiological signals, but also skin hydration measured by impedance sensors [13–15] (e.g., Fig. 2.1e [13]) and skin temperature by resistance temperature detectors (e.g., Fig. 2.1f [16]) are well compared to gold standards. However, not all motions should be excluded from epidermal sensors. For example, deformation sensitive soft strain gauges are intentionally integrated on epidermal patches to accurately detect respiration from the chest (Fig. 2.1g [17]), pulse wave (Fig. 2.1f [17]) and tremor [18] from the wrist, as well as hand gesture [19] because they are able to closely follow skin deformation. Other than examples displayed in Fig. 2.1, epidermal electronics have also inspired epidermal biochemical sensors [20, 21], skin stiffness sensors [22], wearable antenna for wireless near field communication (NFC) [15, 23, 24], and so on. In summary, epidermal sensors and electronics have been demonstrated as a platform technology with unlimited potential applications.

With so many exciting applications in mind, it is important not to forget that the thinness and softness of epidermal patches would lead to collapsing and crumpling after they are peeled off from human skin, making their ideal use to be disposable devices. As a result, the success of epidermal devices hinges on the realization of low cost, high throughput manufacture, which is going to be the last topic of this chapter.

2.2 Stretchability of Serpentines

Currently, the most popular strategy to build in-plane stretchable circuits and sensors out of intrinsically stiff materials is to pattern the stiff materials into meandering serpentine ribbons [25–28]. When thin serpentines ribbons are stretched, the ribbons can rotate in plane as well as buckle out of plane to accommodate the applied deformation, resulting in greatly reduced strains as well as much lower effective stiffness [26]. In addition to metal [25, 27–32] or graphene interconnects [33], electrophysiological or thermal sensing electrodes [4, 9, 12, 16], microheaters [18, 34], silicon-based solar cells and amplifiers [4], as well as zinc oxide-based nanogenerators [35] can all be patterned into serpentine shapes using conventional photolithography and etching methods [4, 28, 33]. Except for polymer-bonded serpentines, freestanding stretchable serpentine network has been applied in deployable sensor networks [36, 37] and expandable coronary stents [38]. In these two cases, the serpentine thickness is much larger than the ribbon width, and the expandability just comes from in-plane rigid body rotation of the serpentine arms. Although serpentines are so popular, their stretchability vary over a wide range and their designs lack rational guidance. According to the existing studies, the applied strain-to-rupture of metallic serpentine ribbons varies from 54 to 1600 % [25, 27–

29, 32, 36], depending on the geometric parameters such as ribbon width, arc radius, arm length substrate support, and so on. To obtain a fundamental understanding of their effects, and to optimize their layout under practical constraints, we have performed systematic theoretical, numerical, and experimental studies, as discussed in the follows.

2.2.1 *Freestanding, Non-buckling Serpentines*

It is possible to obtain analytical solutions to freestanding, non-buckling serpentine ribbons through curved beam (CB) theory and elasticity theory, as shown in Fig. 2.2 [39, 40]. Figure 2.2a depicts a unit cell cut out of a one-directional periodic serpentine ribbon whose geometry can be completely defined by four parameters: the ribbon width w, the arc radius R, the arc angle α, and the arm length l. The end-to-end distance of a unit cell is denoted by S, which is a function of the four basic parameters. When this unit cell is subjected to a tensile displacement u_0 at each end, the effective applied strain ε_{app} is defined as

$$\varepsilon_{\text{app}} = \frac{2u_0}{S}. \tag{2.1}$$

Therefore a straight ribbon (i.e. $\alpha = -90°$) of length S should experience a uniform strain of ε_{app} everywhere inside the ribbon if the end effects are neglected. Taking advantage of symmetry, a unit cell can ultimately be represented by a quarter cell with fixed boundary at the axis of symmetry and a displacement of $u_0/2$ at the end, as shown in Fig. 2.2b. The reaction force is named P in Fig. 2.2b. Assuming linear elastic material and small deformation, through CB theory, the normalized stiffness and maximum strain in the serpentine can be obtained analytically as [39]:

$$\frac{P}{P'} = \frac{\frac{w}{R}\left(\cos\alpha - \frac{l}{2R}\sin\alpha\right)}{2\left[\begin{array}{c}\cos^2\alpha\left(\frac{l^3}{2R^3} + 3\left(\frac{\pi}{2}+\alpha\right)\frac{l^2}{R^2} + 12\frac{l}{R} - 12\left(\frac{\pi}{2}+\alpha\right)\right) \\ + \sin 2\alpha\left(6\left(\frac{\pi}{2}+\alpha\right)\frac{l}{R} + 9\right) \\ + \frac{w^2}{R}\left[\left(\frac{\pi}{2}+\alpha\right)\left(\frac{l}{2R}\cos\alpha + \sin\alpha\right)^2 + \frac{l}{2R}\left(\sin\alpha + \frac{3\overline{E}}{2G}\cos\alpha\right)\right] + 18\left(\frac{\pi}{2}+\alpha\right)\end{array}\right]}, \tag{2.2}$$

where $P' = 2\overline{E}wu_0/S$ represents the reaction force needed for the linear counterpart of the serpentine to elongate by $2u_0$, and

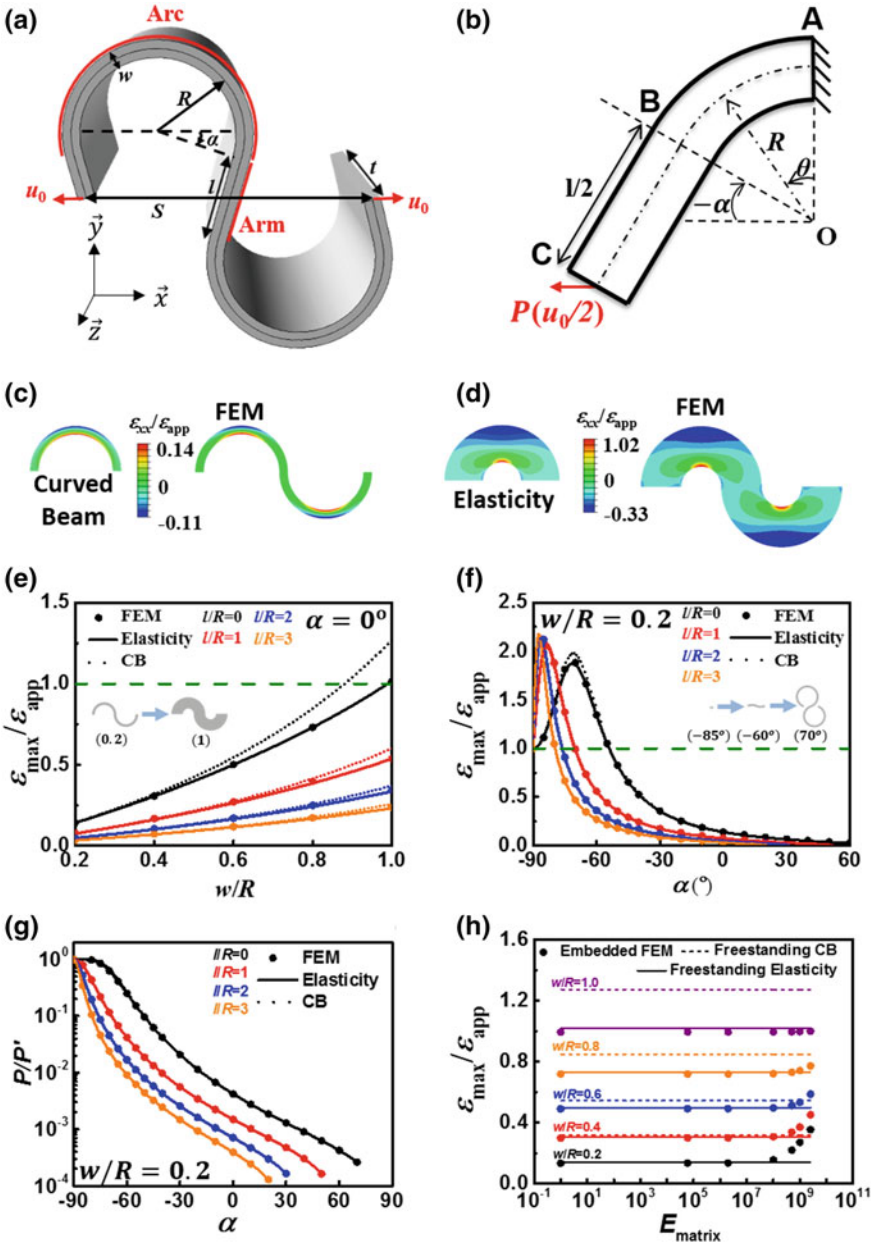
(a)
Arc
w
R
α
u0
l
s
t
Arm
u0
y
x
z
(b)
A
B
R
θ
l/2
−α
C
O
P(u0/2)
(c)
Curved Beam
εxx/εapp
0.14
0
-0.11
FEM
(d)
Elasticity
εxx/εapp
1.02
0
-0.33
FEM
(e)
FEM
Elasticity
CB
l/R=0
l/R=1
l/R=2
l/R=3
α = 0°
(0.2)
(1)
εmax/εapp
w/R
(f)
w/R = 0.2
l/R=0
l/R=1
l/R=2
l/R=3
FEM
Elasticity
CB
(−85°) (−60°) (70°)
εmax/εapp
α(°)
(g)
l/R=0
l/R=1
l/R=2
l/R=3
FEM
Elasticity
CB
w/R = 0.2
P/P'
α
(h)
Embedded FEM
Freestanding CB
Freestanding Elasticity
w/R=1.0
w/R=0.8
w/R=0.6
w/R=0.4
w/R=0.2
εmax/εapp
Ematrix

◀ **Fig. 2.2** 2D plane strain model of non-buckling freestanding and polymer-embedded serpentines [39, 40]. **a** Geometric parameters and boundary conditions of the unit cell of a freestanding serpentine ribbon. **b** Simplified model due to symmetry. **c** Comparison between curved beam (CB) theory and FEM results of strain distribution in a narrow serpentine. **d** Comparison between elasticity theory and FEM results of strain distribution in a wide serpentine. **e** Normalized maximum strain in the serpentine is plotted as a function of normalized ribbon width for serpentines with various arm lengths, which suggests smaller width and longer arms yield lower strains. **f** Normalized maximum strain in the serpentine is plotted as a function of arc angle for various arm lengths, which suggests nonmonotonic arc angle effect and that some serpentines can develop higher strains than straight ribbons. **g** Serpentine stiffness normalized by its linear counterpart is plotted as a function of arc angle for various arm lengths, which indicates that there can be orders of magnitude reduction when patterning straight ribbons into serpentine shapes. **h** Normalized maximum strain in an embedded serpentine as a function of matrix modulus, which suggests that analytical solutions to freestanding serpentines is valid for serpentines embedded in soft polymer matrix (e.g., $E_{\text{matrix}} < 100$ MPa)

$$\frac{\varepsilon_{\max}}{\varepsilon_{\text{app}}} = \frac{\frac{w}{R}\left[\frac{12}{2-\frac{w}{R}} + \left(\frac{12}{2-\frac{w}{R}} - \frac{w}{R}\right)\left(\sin\alpha + \frac{l}{2R}\cos\alpha\right)\right]\left(\cos\alpha - \frac{l}{2R}\sin\alpha\right)}{\left[\begin{array}{c}\cos^2\alpha\left(\frac{l^3}{2R^3} + 3\left(\frac{\pi}{2}+\alpha\right)\frac{l^2}{R^2} + 12\frac{l}{R} - 12\left(\frac{\pi}{2}+\alpha\right)\right) \\ + \sin 2\alpha\left(6\left(\frac{\pi}{2}+\alpha\right)\frac{l}{R} + 9\right) \\ + \frac{w^2}{R}\left[\left(\frac{\pi}{2}+\alpha\right)\left(\frac{l}{2R}\cos\alpha + \sin\alpha\right)^2 + \frac{l}{2R}\left(\sin\alpha + \frac{3\overline{E}}{2G}\cos\alpha\right)\right] + 18\left(\frac{\pi}{2}+\alpha\right)\end{array}\right]}. \tag{2.3}$$

Such closed-form analytical results have found excellent agreement with finite element modeling (FEM) results as shown in Figs. 2.3c, e–g, as long as the serpentine width is small enough compared to its arc radius, e.g., $w/R < 0.5$. According to the contour plots of strain distribution in Fig. 2.3c, it is obvious that the maximum strain always occurs at the inner crest of the arc, which is exactly where fracture occurred in our experiments [39]. It is evident in Fig. 2.3e that serpentines with smaller width and longer arms exhibit lower maximum strains and hence better stretchability. Figure 2.3e also suggests that the CB solutions (dashed curves) match the FEM results (solid markers) well when $w/R < 0.5$. To obtain accurate solutions for wide serpentines, we recently developed the elasticity solution [40] whose contour plot is compared with FEM in Fig. 2.3d and strain and stiffness results are plotted as solid curves in Figs. 2.3e–h. Through the comparison, it is evident that elasticity solution can fully capture the FEM results for all ribbon widths. Unfortunately, unlike the CB solution, the elasticity solutions cannot be expressed as short equations. The effect of the arc angle α is illustrated by Fig. 2.3f. Two observations can be readily made: first, while the effects of w/R and l/R are monotonic, the effect of α is not always monotonic; second, when α is close to $-90°$, i.e., when the serpentine approaches a straight ribbon, the maximum strain in the serpentine may exceed the applied strain, meaning the serpentine is less stretchable compared with their straight counterpart. As a result, it is important for us to realize that not all serpentines can help reduce strains and the design of the serpentine needs to be rationalized. Fig. 2.3g plots the effective stiffness of the

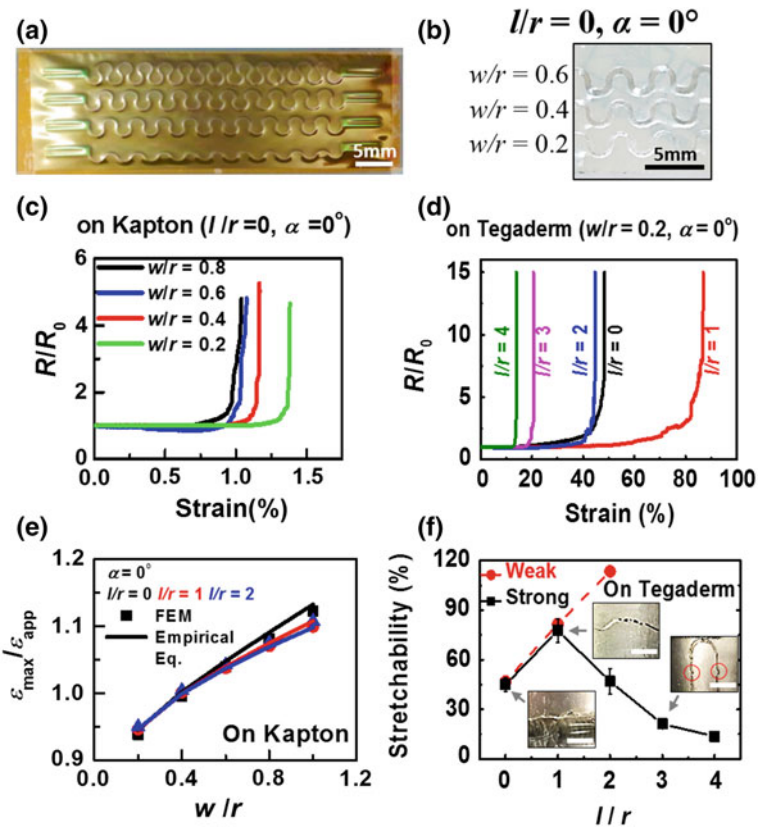

Fig. 2.3 Experiments of brittle ITO serpentines supported by stiff [50] and soft [51] polymer substrates. **a** Top view of ITO serpentines directly sputtered on a Kapton substrate through a stencil. **b** Top view of transparent ITO-PET serpentines transfer printed on a Tegaderm substrate. **c** Resistance of ITO serpentines of different widths measured when Kapton is pulled by uniaxial tensile strain, which indicates that ITO serpentines on stiff polymer like Kapton are not very stretchable. **d** Resistance of ITO serpentines of different arm lengths measured when Tegaderm is pulled by uniaxial tensile strain, which indicates much enhanced stretchability. **e** Normalized FEM maximum strain in Kapton-supported serpentine as a function of normalized serpentine width. **f** Measured stretchability of Tegaderm-supported serpentine as a function of serpentine arm length

serpentines normalized by that of a straight ribbon. It is impressive that the effective stiffness can be reduced by orders of magnitude by simply changing a straight ribbon into serpentine shapes—this is why metal or silicon-based serpentines can be made as soft as skins [4] and tissues [41].

When thick, non-buckling serpentines of stiff metal are embedded in a polymer matrix [25], we have performed FEM to reveal their ε_{max} when ε_{app} is applied to pull the polymer matrix. Figure 2.3h plots $\varepsilon_{max}/\varepsilon_{app}$ as a function of the matrix modulus E_{matrix} against the CB (dashed line) and elasticity (solid line) solutions for freestanding serpentines, which are flat because they are independent of E_{matrix}.

When E_{matrix} < 100 MPa, the FEM results fall right on the analytical solutions for freestanding serpentines, which indicates that soft polymer matrix has almost no effect on the deformation of non-buckling serpentine. Hence the strain in metal serpentines embedded in polydimethylsiloxane (PDMS) (e.g., 10:1 Sylgard 184 PDMS has a Young's modulus of 3 MPa [42]) can be well captured by the analytical solutions for freestanding serpentines when metal deformation is within the elastic regime.

When serpentine ribbons' thickness is much smaller compared to their width, as in most epidermal sensors, freestanding serpentines will buckle out of plane to avoid in-plane bending by developing out-of-plane bending and twisting, which stores much lower strain energy. Buckling and postbuckling theories and FEM have been developed to address this problem [26, 43, 44]. To enhance the areal coverage of functional serpentines without compromising the multidirectional stretchability, a concept of self-similar or fractal serpentines have been proposed, which has also greatly enhanced the topologies of serpentine designs [24, 32, 45, 46]. So far, the optimization theories for freestanding and interlaced serpentine networks are still lacking.

2.2.2 Substrate-Supported Serpentines

The mechanical behaviors of polymer-bonded serpentines are expected to be very different from the freestanding ones. A few experiments and FEM have been conducted to provide insights into the shape-dependent mechanical behaviors of polymer-supported metal-based serpentines [27–30, 36, 47–49]. Other than metallic serpentines, ceramic serpentines start to gain popularity as stretchable solar cells [4], amplifiers [4], and nanogenerators [35]. But so far there is little experimental mechanics investigation to reveal the stretchability of polymer-bonded brittle serpentine thin films due to the difficulty to fabricate and handle brittle serpentines on soft polymer substrates. We have used indium tin oxide (ITO) as a model brittle material to study the mechanics of polymer-bonded brittle serpentines [50, 51].

Thin ITO films have been a popular electrode material in flat panel displays [52] and solar cells [53] attributing to their combined high electrical conductivity and optical transparency. However, ITO is not mechanically favorable in flexible/stretchable electronics due to its brittle nature. Cracks were observed at applied tensile strains around 1 % in polymer-supported blanket thin ITO films [38, 54]. Resistance versus applied strain curves have been widely adopted to indicate the stretchability of conductive thin films such as metal [55–57] and ITO [38]. We have sputtered ITO serpentines on Kapton® (DuPont) substrates through stencils as shown in Fig. 2.3a [50] and "cut-and-pasted" ITO-PET (polyethylene terephthalate) bilayer serpentines on soft stretchable Tegaderm® (3M medical tape) substrates as displayed in Fig. 2.3b [51]. Through the measurement of electrical resistance as a function of tensile strain applied to the substrate (Fig. 2.3c for ITO on Kapton and Fig. 2.3d for ITO-PET on Tegaderm), the strain-to-rupture (a.k.a. stretchability) can be determined as the strain at which the resistance starts to blow up.

A series of FEMs are performed for systematically varied serpentine shapes when the substrate is Kapton (E_{Kapton} = 2.5 GPa). An empirical equation is fitted based on the FEM results as discussed in [50]. Figure 2.3e plots $\varepsilon_{max}/\varepsilon_{app}$ as a function of w/r with different l/r using both the FEM results and the empirical equation. It is evident that w/r always has a monotonic effect on $\varepsilon_{max}/\varepsilon_{app}$—smaller strains in narrower ribbons. Another important finding is that when w/r is beyond about 0.4, $\varepsilon_{max}/\varepsilon_{app}$ will go beyond 1, which means the stretchability of the serpentine will actually be lower than its straight counterpart, indicating a strain augmentation instead of strain reduction effect. Compared with the effect of w/r, the effects of arm length l/r and α (not shown) are not as significant, especially when w/r is small. The fundamental reason is that the in-plane rotation and out-of-plane buckling/twisting of the serpentine ribbons are fully constrained by the stiff polymer substrates. Hence we conclude that stiff serpentines directly bonded to stiff polymer substrates like Kapton or PET are in general not much more stretchable than their linear counterpart and many shapes actually can be even worse.

Brittle serpentines are expected to be more stretchable when bonded to a very soft substrate like the Tegaderm ($E_{Tegaderm}$ = 7 MPa [58]) because the constraint from the substrate is much reduced. However, directly sputtering thin ITO films on elastomeric substrates resulted in surface wrinkles [59] and from our own experience, ITO films easily cracked with even very gentle handling. The idea we came up with is to first sputter ITO on transparent PET sheet and then transfer ITO-coated PET serpentines on Tegaderm [51]. Depending on serpentine shape and adhesion to the Tegaderm substrate, ITO ribbons can remain conductive when stretched beyond 100 %, as shown in Fig. 2.3f. Generally speaking, weakly-bonded serpentines debond from the substrate before rupture, and are always more stretchable with narrower ribbon width, longer arms, larger arc radius, and larger arc angle. The stretchability of well-bonded serpentines, however, show non-monotonic dependence on those geometric parameters due to stronger substrate constraints. It is found that serpentines with long arms rupture by transverse buckling due to Poisson's contraction in Tegaderm, which degrades stretchability when the transverse dimension is large.

2.3 Conformability of Epidermal Sensors on Rough Skin Surfaces

Noninvasive but intimate contact with epidermis is required for superior signal-to-noise ratio and suppressed motion artifacts in epidermal electrophysiological (EP) sensors, hydration sensors, and mechanical sensors [4, 9, 12, 13, 22]. Moreover, conformability-enabled efficient heat and mass transfer between device and skin has led to very precise skin temperature detectors [16], low power wearable heaters [60, 61], effective sweat monitors [20, 62], and on demand drug delivery patches [18]. A comprehensive mechanistic understanding on the

conformability of thin device sheets on rough epidermis can offer important insights into the design of the mechanical properties of epidermal devices.

Conformability between epidermal electronics and skin has been analytically studied through the energy minimization method [63, 64], which can successfully predict non-conformed and fully conformed scenarios. Jeong et al. [12] carried out a series of experiments to study the conformability of elastomer membranes (Ecoflex, Smooth-On, USA) on an Ecoflex skin replica. Membrane-substrate conformability is clearly revealed by the cross-sectional scanning electron microscopy (SEM) images as displayed in Fig. 2.4a [12]: 5 μm thick patch achieved full conformability to the substrate, 36 μm thick one only partially conformed to the substrate, whereas patches with thickness of 100 μm and 500 μm remained non-conformed at all. For illustration purpose, 2D schematics for fully conformed (FC), partially conformed (PC), and non-conformed (NC) scenarios are offered in Fig. 2.4b–d, respectively. We therefore developed an extended theory that can

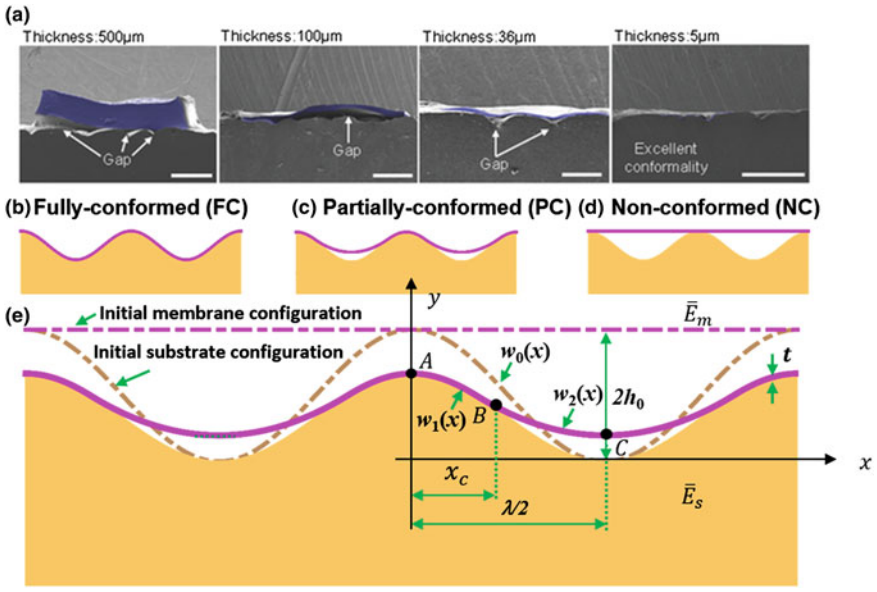

Fig. 2.4 Illustration of epidermal device conforming to rough skin surface. **a** Cross-sectional SEM pictures showing 5 μm Ecoflex is fully conformed to Ecoflex-based skin replica, 36 μm one achieved partial conformability, whereas 100 μm and 500 μm ones did not conform at all [12]. **b–d** offer schematics of fully conformed (FC), partially conformed (PC), and non-conformed (NC) scenarios. **e** Schematic of a generic partially conformed membrane with geometric parameters and characteristic points labeled: the initial amplitude and wavelength of the substrate is $2h_0$ and λ, respectively; after membrane lamination, the substrate surface within the contact zone deforms to a new sinusoidal shape with amplitude $2h_1$ (not labeled in the figure) and unchanged wavelength; x_c is the horizontal projection of the contact zone; Point B denotes the delaminating point

predict all three scenarios by successfully finding the substrate elastic energy under partially conformed contact [65].

A 2D schematic for a generic partially conformed configuration is given in Fig. 2.4e. For simplicity, the membrane is modeled as a uniform linear elastic membrane with plane strain modulus $\overline{E}_m$ and thickness t. The skin is assumed to be a pre-corrugated linear elastic half space with plane strain modulus $\overline{E}_s$. Within the Cartesian coordinate system xy defined in Fig. 2.4e, the surface profile of the undeformed skin as outlined by the dashed peachpuff curve is simply characterized by a sinusoidal function $w_0(x)$ with amplitude $2h_0$ and wavelength λ. When the elastic membrane is laminated on the skin substrate and starts to conform to the substrate due to interface adhesion, a contact zone with horizontal projection denoted as x_c is labeled in Fig. 2.4e. Therefore $x_c = \lambda/2$ represents FC scenario (Fig. 2.4b), $0 < x_c < \lambda/2$ PC scenario (Fig. 2.4c), and $x_c = 0$ NC scenario (Fig. 2.4d). Due to membrane-substrate interaction, the skin substrate deforms. Here, we simply postulate that the surface profile of the skin within the contact zone deforms from the initial sinusoidal shape $w_0(x)$ to a new sinusoidal shape $w_1(x)$ (within $0 \le x \le x_c$) with the same wavelength but a different amplitude, $2h_1$. This assumption holds all the way till $x_c = \lambda/2$, which means the overall skin surface deforms from one sinusoidal profile to another with the same wavelength but different amplitude. The profile of a partially conformed membrane, $w_2(x)$ as illustrated by the magenta curve in Fig. 2.4e is sectional: from A to B, i.e., when $0 \le x \le x_c$, the membrane fully conforms to the substrate and thus $w_2(x) = w_1(x)$; from B to C, i.e., when $x_c \le x \le \lambda/2$, the membrane is suspended and $w_2(x)$ is assumed to be a hyperbolic shape which will decay to a parabolic shape when normal strain in the membrane is small, i.e., a pure bending condition is assumed [66, 67].

To solve for x_c and h_1, energy minimization method is adopted. The total energy per period of the system, U_{total}, consists of the following four energies:

$$U_{\text{total}} = U_{\text{bending}} + U_{\text{membrane}} + U_{\text{adhesion}} + U_{\text{substrate}}, \tag{2.4}$$

where U_{bending} is the bending energy of the membrane, U_{membrane} is the membrane energy associated with tensile strain in the membrane, U_{adhesion} is the interface adhesion energy between the membrane and the substrate which is proportional to the interface work of adhesion, γ, and $U_{\text{substrate}}$ is the elastic energy stored in the substrate, which equals to the work done to the substrate by the membrane.

Detailed derivations of the four energies yielded four dimensionless governing parameters for this problem [65]: $\beta = 2\pi h_0/\lambda, \eta = t/\lambda, \alpha = \overline{E}_m/\overline{E}_s$, and $\mu = \gamma/(\overline{E}_s\lambda)$, which are physically interpreted as normalized roughness of the corrugated skin surface (β), normalized membrane thickness (η), membrane-to-substrate modulus ratio (α), and normalized membrane-substrate interface adhesion (μ), respectively. In addition, there are two unknown dimensionless parameters: $\widehat{x}_c = 2x_c/\lambda$ and $\xi = h_1/h_0$, which once solved can yield the contact zone size and the amplitude of the deformed substrate. By fixing $\beta, \alpha, \mu,$ and η, minimization of

Eq. (2.4) with respect to $\widehat{x}_c$ and ξ within the domain confined by $0 \le \widehat{x}_c \le 1$ and $0 \le \xi \le 1$ will give us the equilibrium solution, which can be visualized as the global minimum of a 3D plot of the normalized total energy landscape as a function of $\widehat{x}_c$ and ξ.

Our analytical solutions can be directly compared with Jeong's conformability experiment [12]. Basic parameters that can be extracted from the experiment are: substrate roughness $h_0 = 50\,\mu\text{m}, \lambda = 250\,\mu\text{m}$, plane strain moduli of Ecoflex membrane and substrate $\overline{E}_s = \overline{E}_m = 92\,\text{KPa}$ [4]. The interface work of adhesion is taken as $\gamma = 50\,\text{mJ/m}^2$ according to our recent experimental measurements of elastomer adhesion [42]. Based on those given parameters, the four dimensionless parameters are computed as: $\beta = 1.2, \alpha = 1, \mu = 0.003$, and $\eta = 0.02$, 0.144, 0.04, and 2, which corresponds to the four different experimental thicknesses of the membrane t = 5, 36, 100, 500 μm, respectively. By fixing the substrate morphology $\beta = 1.2$ (i.e., $h_0 = 50\,\mu\text{m}, \lambda = 250\,\mu\text{m}$), Fig. 2.5 predicts the conformability as a function of the other three parameters α, μ and η. The 3D plot in Fig. 2.5a shows two critical surfaces dividing FC/PC and PC/NC. The conclusion is consistent with

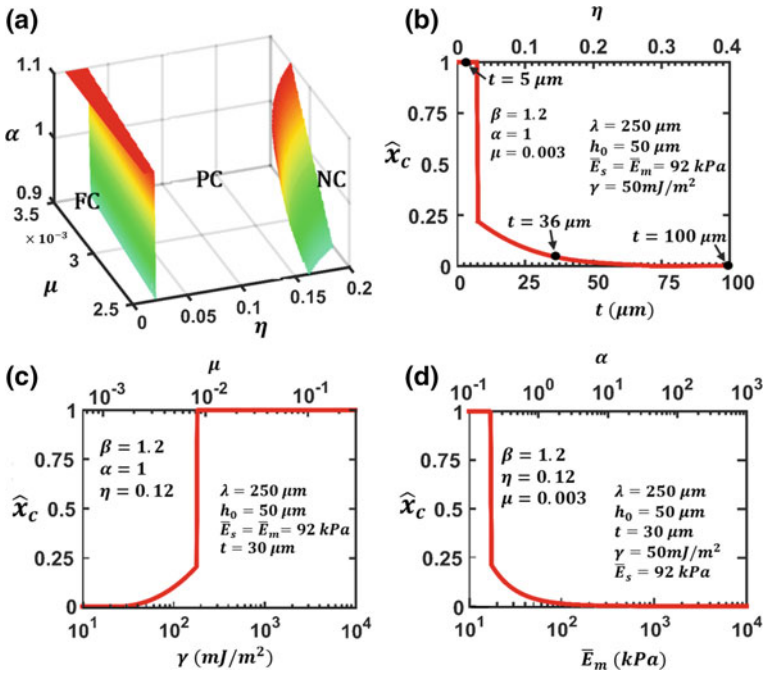

Fig. 2.5 Conformability prediction when fixing skin surface roughness: $h_0 = 50\,\mu\text{m}, \lambda = 250\,\mu\text{m}$ [65]. **a** Surfaces dividing FC/PC and PC/NC. **b** Contact area $\widehat{x}_c$ versus t (or η) when $\beta = 1.2, \alpha = 1, \mu = 0.003$, which agrees well with Jeong's experiments [12] (labeled as black dots). **c** Contact area $\widehat{x}_c$ versus γ (or μ) when $\beta = 1.2, \alpha = 1, \eta = 0.12$. **d** Contact area $\widehat{x}_c$ versus $\overline{E}_m$ (or α) when $\beta = 1.2, \mu = 0.003, \eta = 0.12$

our intuition that the FC condition can be achieved at small η, i.e., thin membrane, small α, i.e., compliant membrane, and large μ, i.e., strong membrane-substrate adhesion. On the contrary, NC condition occurs at large α, large η, and small μ.

To better illustrate the effect of individual variables, we chose to fix three variables and only change one at a time. For example, in Fig. 2.5b, $\widehat{x}_c$ is plotted as a function of t in the bottom axis and η in the top axis with $\beta = 1.2, \alpha = 1, \mu = 0.003$ fixed. It is evident that as the film thickness grows from 0, the conformability goes from FC to PC and finally NC. While the transition from PC to NC is smooth, the transition from FC to PC is abrupt, which suggests a significant drop (>77 %) of contact area from FC to PC. Similar jumps have been observed for few layer graphene (FLG) conforming to silicon substrate [68] and elastic membrane laminated on rigid, corrugated substrate [66]. More analysis on how different substrate morphologies affect snap-through transition of conformability can be found in [67]. Quantitatively, full conformability requires $\eta < 0.03$, i.e., $t < 7.5\,\mu\text{m}$. When $\eta > 0.28$, i.e., $t > 70\,\mu\text{m}$, there is no conformability at all. When $0.03 < \eta < 0.28$, i.e., when $7.5\,\mu\text{m} < t < 70\,\mu\text{m}$, the contact area of the PC scenario can be determined. The three black dots in Fig. 2.5b indicate the three different membrane thicknesses tested in the Jeong's experiment [12], which are fully consistent with our prediction.

Since the original epidermal electronics was fabricated on 30 μm thick Ecoflex [4], the conformability of a 30 μm thick Ecoflex on an Ecoflex skin replica has been predicted. In order to show the effect of adhesion energy and membrane modulus over wide ranges, $\widehat{x}_c$ versus γ (or μ) and $\widehat{x}_c$ versus $\overline{E}_m$ (or α) are plotted with log$x$ scale in Figs. 2.5c, d, respectively, with the rest three variables fixed. In Fig. 2.5c, it is evident that when $\mu > 0.008$, i.e., $\gamma > 138\,\text{mJ/m}^2$, FC mode can be achieved but when $\mu < 0.0016$, i.e., $\gamma < 30\,\text{mJ/m}^2$, the membrane would not conform to the substrate at all. Figure 2.5d indicates that when $\alpha < 0.2$, i.e., $\overline{E}_m < 10\,\text{kPa}$, FC is guaranteed but when $\alpha > 2.5$, i.e., $\overline{E}_m > 125\,\text{kPa}$, there is no conformability. It is also noted that the abrupt transition from FC to PC is also present in Fig. 2.5c, d, with the same maximum contact area (23 % of total surface area) under PC. In summary, Fig. 2.5 offers a quantitative guideline toward conformable skin-mounted electronics in a four-dimensional design space.

2.4 "Cut-and-Paste" Manufacture of Epidermal Sensors

Disposable and widely accessible epidermal sensors rely on the realization of low cost, high throughput manufacture. Current manufacture leverages standard microelectronics fabrication processes including vacuum deposition of films, spin coating, photolithography, wet and dry etching, as well as transfer-printing [4, 23, 69]. Although it has been proved effective, it requires access to cleanroom facilities and the time and labor costs are burdensome. Plus the overall size of the device is limited to the scale of the rigid handling wafer.

Our newly invented "cut-and-paste" method offers a very simple and immediate solution to these limitations [58]. Instead of vacuum deposition, thin metal-on-polymer laminates of various thicknesses can be directly purchased from industrial manufacturers. Instead of using photolithography patterning, a benchtop electronic cutter plotter is used to mechanically carve out the designed patterns, with excess being removed, which is a freeform, subtractive manufacturing process, inverse to the popular freeform, additive manufacturing technology [70]. The cutter plotter can pattern on thin sheet metals and polymers up to 12 inches wide and several feet long, largely exceeding lab-scale wafer sizes. Since the patterns can be carved with the support of thermal release tapes (TRT), the patterned films can be directly printed onto a variety of tattoo adhesives and medical tapes with almost 100 % yield. The whole process can be completed on an ordinary bench without any wet process within 10 min, which allows rapid prototyping. Equipment used in this process only includes a desktop cutter plotter and a hot plate for TRT heating, which enables portable manufacture. Since no rigid handle wafer is needed throughout the process, the "cut-and-paste" method is intrinsically compatible with roll-to-roll manufacture. The only drawback of this method is the limited patterning resolution of state-of-the-art cutter plotters, which is universally around 200 μm.

The detailed "cut-and-paste" process is illustrated in Fig. 2.6 [58]. Since thin metal films supported by stiff polymers such as Kapton and PET are more stretchable than freestanding metal foils [55], we always use metal-PET laminates

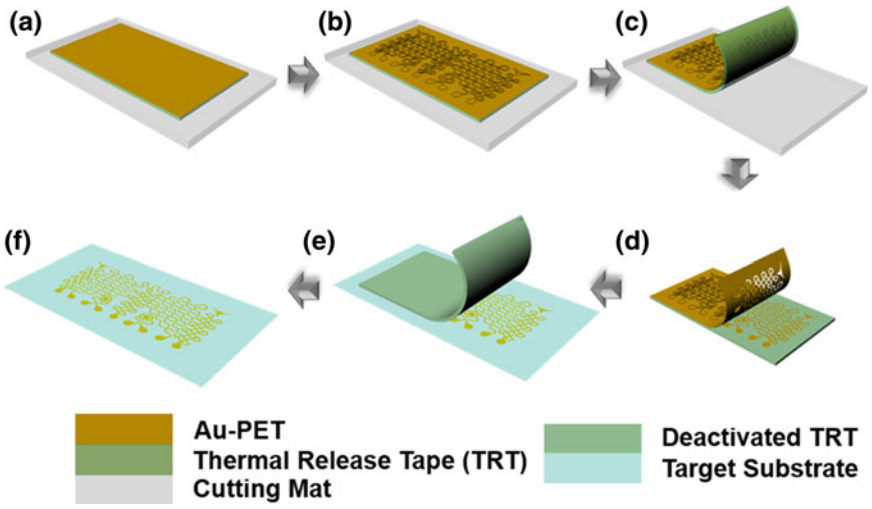

Fig. 2.6 Schematics for the cost and time effective "cut-and-paste" process [58]. **a** Au-PET-TRT (APT) laminated on the cutting mat with PET being the topmost layer. **b** Carving designed seams in the Au-PET layer by an automated cutter plotter. **c** Peeling APT off from the cutting mat. **d** Removing excessive Au-PET flakes after deactivating the TRT on hot plate. **e** Printing patterned Au-PET onto target substrate. **f** Resulted epidermal sensor systems with Au being the topmost layer. Steps (**a**)–(**e**) can be repeated for other materials

as the starting materials, which can be readily purchased from industrial suppliers such as Sheldahl (Northfield, MN) and Neptco (Pawtucket, RI). To manufacture gold (Au)-based stretchable electrophysiological (EP) electrodes, resistance temperature detectors (RTD), and impedance sensors, 100 nm-Au-on-13 μm-PET sheet was uniformly bonded to a flexible, single-sided TRT (Semiconductor Equipment Corp., USA) with Au side touching the adhesive of the TRT. The other side of the TRT was then adhered to a tacky flexible cutting mat, as shown in Fig. 2.6a. The cutting mat was fed into an electronic cutter plotter (Silhouette Cameo, USA) with the PET side facing the cutting blade. By importing our AutoCAD design into the Silhouette Studio software, the cutter plotter can automatically carve the Au-PET sheet with designed seams within minutes (Fig. 2.6b). Once seams were formed, the TRT was gently peeled off from the cutting mat (Fig. 2.6c) and slightly baked on a 115 °C hotplate for 1–2 min. Heat deactivated the adhesives on the TRT such that the excessive flakes can be easily peeled off by tweezers (Fig. 2.6d), leaving only the desired device patterns loosely resting on the TRT. The patterned devices were finally printed on a target substrate with native adhesives, which could be a temporary tattoo paper (Silhouette) or a medical tape, such as the 3M Tegaderm transparent dressing or the 3M kind removal silicone tape (KRST) (Fig. 2.6e), yielding a Au-based epidermal sensing patch (Fig. 2.6f). Steps illustrated by Figs. 2.6a–e can be repeated for other thin sheets of metals and polymers, which can be printed on the same target substrate with alignment markers, rendering a multimaterial, multiparametric epidermal sensing patch ready for skin mounting.

To demonstrate the "cut-and-paste" method, multimaterial epidermal sensor systems are fabricated and applied to measure EP signals such as ECG (Fig. 2.7a), EMG (Fig. 2.7b), and electroencephalogram (EEG) (Fig. 2.7c), skin temperature (Fig. 2.7d), skin hydration (Fig. 2.7e), and respiratory rate (Fig. 2.7f). Those measurements are compared favorably to state-of-the-art gold standards. Except that the soft strain gauges for respiratory rate sensing are made out of electrically conductive rubber (ECR)(Elastosil LR 3162, Wacker Silicones), all other sensors are Au-based passive sensors. In addition to sensors, a planar stretchable coil of 9 μm-Al-13 μm-PET ribbons exploiting the double-stranded serpentine design is also integrated on the same patch as a low frequency, wireless strain gauge, which can also serve as NFC antenna in the future.

Note that the above mentioned "cut-and-paste" method has proved effective in patterning metal-on-polymer laminates and elastomeric sheets, but it is not directly applicable to ceramic-coated polymer as indentation of the cutting blade would easily shatter intrinsically brittle ceramic film. However, the stretchable ITO-PET serpentines on Tegaderm shown in Fig. 2.3b were fabricated through a variation of the "cut-and-paste" method [51]. Instead of cutting blanket ITO-PET sheets, we first cut on a bare PET sheet, deposited thin ITO film on the cut PET (ITO deposited over the seam trenches are discontinuous), and then removed the excessive. In this way, no cutting is performed on ITO and the pattern in the ITO-PET bilayer is formed by a process very similar to the "lift-off" process in microfabrication. ITO is just one example of brittle materials. Such a cost and time effective process can also be applied to pattern other brittle materials.

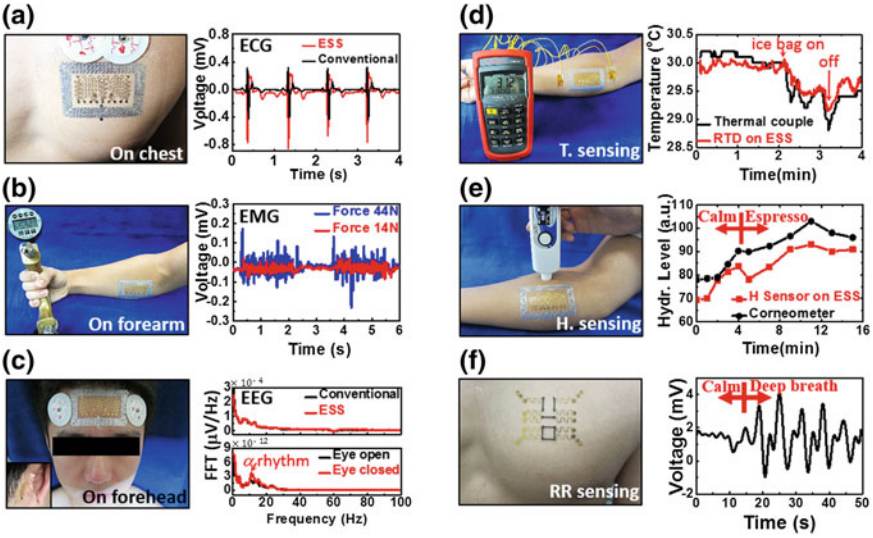

Fig. 2.7 ECG, EMG, EEG, skin temperature, skin hydration, and respiratory rate measurements by low-cost epidermal sensors [58]. **a** ECG simultaneously measured by ESS (*red*) and Ag/AgCl gel electrodes (*black*). Stronger ECG signals were obtained by the epidermal electrodes. **b** Epidermal electrodes attached on human forearm for EMG measurement when the subject is gripping a commercial dynamometer with different forces. Higher EMG amplitude corresponded to higher gripping force. **c** EEG measured on human forehead by both epidermal electrodes and Ag/AgCl gel electrodes. Two frequency spectrums of the EEG are well overlapped. 10 Hz alpha rhythm measured by epidermal electrodes is clearly visible when eyes were closed. **d** Skin temperature changes measured by both epidermal resistance temperature detector (RTD) and thermocouple found good correlation. **e** Real-time skin hydration before and after Espresso intake measured by both commercial corneometer and epidermal impedance sensor. **f** Voltage outputs from the electrically conductive rubber (ECG)-based Wheatstone bridge during normal and deep breath

2.5 Conclusions

This chapter presents our recent studies on the stretchability, conformability, and low-cost manufacture of epidermal sensors, which is a compelling example of bio-integrated electronics. After a decade of development, the intrinsic stiffness and brittleness of electronic materials is no longer a road block to stretchable electronics. We want to emphasize that in addition to stretchability of the sensors, conformability to soft but rough tissue surface is another key requirement for bio-integrated electronics. While examples in this chapter are based on metal and ceramic materials, the fundamental mechanics and ubiquitous "cut-and-paste" manufacturing process are also applicable to other classes of materials. Except epidermal applications, soft sensor and electronic sheets have also found many other exciting applications *in vivo* as well as in tissue engineering, and there will be many more to come.

References

1. D.H. Kim, R. Ghaffari, N.S. Lu, J.A. Rogers, Flexible and stretchable electronics for bio-integrated devices. Annu. Rev. Biomed. Eng. **14**, 113–128 (2012)
2. D.H. Kim, N.S. Lu, R. Ghaffari, J.A. Rogers, Inorganic semiconductor nanomaterials for flexible and stretchable bio-integrated electronics. NPG Asia Materials **4**, e15 (2012)
3. J. van den Brand, M. de Kok, A. Sridhar, M. Cauwe, R. Verplancke, F. Bossuyt, et al., Flexible and stretchable electronics for wearable healthcare, in *Proceedings of the 2014 44th European Solid-State Device Research Conference* (Essderc, 2014), pp. 206–209
4. D.H. Kim, N.S. Lu, R. Ma, Y.S. Kim, R.H. Kim, S.D. Wang et al., Epidermal electronics. Science **333**, 838–843 (2011)
5. Z.G. Suo, Mechanics of stretchable electronics and soft machines. MRS Bull. **37**, 218–225 (2012)
6. N. Lu, S. Yang, Mechanics for stretchable sensors. Curr. Opin. Solid State Mater. Sci. in press (2015)
7. J. Song, Mechanics of stretchable electronics. Curr. Opin. Solid State Mater. Sci. **19**, 160–170 (2015)
8. D.H. Kim, N.S. Lu, Y.G. Huang, J.A. Rogers, Materials for stretchable electronics in bioinspired and biointegrated devices. MRS Bull. **37**, 226–235 (2012)
9. W.-H. Yeo, Y.-S. Kim, J. Lee, A. Ameen, L. Shi, M. Li et al., Multifunctional electronics: multifunctional epidermal electronics printed directly onto the skin. Adv. Mater. **25**, 2772 (2013)
10. J.S. Lee, J. Heo, W.K. Lee, Y.G. Lim, Y.H. Kim, K.S. Park, Flexible capacitive electrodes for minimizing motion artifacts in ambulatory electrocardiograms. Sensors **14**, 14732–14743 (2014)
11. J.W. Jeong, M.K. Kim, H.Y. Cheng, W.H. Yeo, X. Huang, Y.H. Liu et al., Capacitive epidermal electronics for electrically safe, long-term electrophysiological measurements. Adv. Healthc. Mater. **3**, 642–648 (2014)
12. J.W. Jeong, W.H. Yeo, A. Akhtar, J.J.S. Norton, Y.J. Kwack, S. Li et al., Materials and optimized designs for human-machine interfaces via epidermal electronics. Adv. Mater. **25**, 6839–6846 (2013)
13. X. Huang, W.H. Yeo, Y. Liu, J.A. Rogers, Epidermal differential impedance sensor for conformal skin hydration monitoring. Biointerphases **7**, 52 (2012)
14. X. Huang, H. Cheng, K. Chen, Y. Zhang, Y. Zhang, Y. Liu et al., Epidermal impedance sensing sheets for precision hydration assessment and spatial mapping. IEEE Trans. Biomed. Eng. **60**, 2848–2857 (2013)
15. X. Huang, Y.H. Liu, H.Y. Cheng, W.J. Shin, J.A. Fan, Z.J. Liu et al., Materials and designs for wireless epidermal sensors of hydration and strain. Adv. Funct. Mater. **24**, 3846–3854 (2014)
16. R.C. Webb, A.P. Bonifas, A. Behnaz, Y.H. Zhang, K.J. Yu, H.Y. Cheng et al., Ultrathin conformal devices for precise and continuous thermal characterization of human skin. Nat. Mater. **12**, 938–944 (2013)
17. M.K. Choi, O.K. Park, C. Choi, S. Qiao, R. Ghaffari, J. Kim, et al., Cephalopod-inspired miniaturized suction cups for smart medical skin. Adv. Healthc. Mater. (2015)
18. D. Son, J. Lee, S. Qiao, R. Ghaffari, J. Kim, J.E. Lee et al., Multifunctional wearable devices for diagnosis and therapy of movement disorders. Nat. Nanotechnol. **9**, 397–404 (2014)
19. J. Kim, M. Lee, H.J. Shim, R. Ghaffari, H.R. Cho, D. Son, et al., Stretchable silicon nanoribbon electronics for skin prosthesis. Nat. Commun. **5** (2014)
20. A.J. Bandodkar, D. Molinnus, O. Mirza, T. Guinovart, J.R. Windmiller, G. Valdes-Ramirez et al., Epidermal tattoo potentiometric sodium sensors with wireless signal transduction for continuous non-invasive sweat monitoring. Biosens. Bioelectron. **54**, 603–609 (2014)
21. W. Jia, A.J. Bandodkar, G. Valdes-Ramirez, J.R. Windmiller, Z. Yang, J. Ramirez et al., Electrochemical tattoo biosensors for real-time noninvasive lactate monitoring in human perspiration. Anal. Chem. **85**, 6553–6560 (2013)

22. C. Dagdeviren, Y. Shi, P. Joe, R. Ghaffari, G. Balooch, K. Usgaonkar, et al., Conformal piezoelectric systems for clinical and experimental characterization of soft tissue biomechanics. Nat. Mater. **14** (2015)
23. J. Kim, A. Banks, H. Cheng, Z. Xie, S. Xu, K.-I. Jang, et al., Epidermal electronics with advanced capabilities in near-field communication. Small (2014)
24. J.A. Fan, W.H. Yeo, Y.W. Su, Y. Hattori, W. Lee, S.Y. Jung, et al., Fractal design concepts for stretchable electronics. Nat. Commun. **5** (2014)
25. D.S. Gray, J. Tien, C.S. Chen, High-conductivity elastomeric electronics. Adv. Mater. **16**, 393 (2004)
26. T. Li, Z.G. Suo, S.P. Lacour, S. Wagner, Compliant thin film patterns of stiff materials as platforms for stretchable electronics. J. Mater. Res. **20**, 3274–3277 (2005)
27. D. Brosteaux, F. Axisa, M. Gonzalez, J. Vanfleteren, Design and fabrication of elastic interconnections for stretchable electronic circuits. IEEE Electron Device Lett. **28**, 552–554 (2007)
28. D.H. Kim, J.Z. Song, W.M. Choi, H.S. Kim, R.H. Kim, Z.J. Liu et al., Materials and noncoplanar mesh designs for integrated circuits with linear elastic responses to extreme mechanical deformations. Proc. Natl. Acad. Sci. U.S.A. **105**, 18675–18680 (2008)
29. Y.Y. Hsu, M. Gonzalez, F. Bossuyt, F. Axisa, J. Vanfleteren, I. De Wolf, In situ observations on deformation behavior and stretching-induced failure of fine pitch stretchable interconnect. J. Mater. Res. **24**, 3573–3582 (2009)
30. Y.Y. Hsu, M. Gonzalez, F. Bossuyt, J. Vanfleteren, I. De Wolf, Polyimide-enhanced stretchable interconnects: design, fabrication, and characterization. IEEE Trans. Electron Devices **58**, 2680–2688 (2011)
31. D.H. Kim, N.S. Lu, R. Ghaffari, Y.S. Kim, S.P. Lee, L.Z. Xu et al., Materials for multifunctional balloon catheters with capabilities in cardiac electrophysiological mapping and ablation therapy. Nat. Mater. **10**, 316–323 (2011)
32. S. Xu, Y.H. Zhang, J. Cho, J. Lee, X. Huang, L. Jia, et al., Stretchable batteries with self-similar serpentine interconnects and integrated wireless recharging systems. Nat. Commun. **4** (2013)
33. R.H. Kim, M.H. Bae, D.G. Kim, H.Y. Cheng, B.H. Kim, D.H. Kim et al., Stretchable, transparent graphene interconnects for arrays of microscale inorganic light emitting diodes on rubber substrates. Nano Lett. **11**, 3881–3886 (2011)
34. C.J. Yu, Z. Duan, P.X. Yuan, Y.H. Li, Y.W. Su, X. Zhang et al., Electronically programmable, reversible shape change in two- and three-dimensional hydrogel structures. Adv. Mater. **25**, 1541–1546 (2013)
35. T. Ma, Y. Wang, R. Tang, H. Yu, H. Jiang, Pre-patterned ZnO nanoribbons on soft substrates for stretchable energy harvesting applications. J. Appl. Phys. **113** (2013)
36. G. Lanzara, N. Salowitz, Z.Q. Guo, F.K. Chang, A spider-web-like highly expandable sensor network for multifunctional materials. Adv. Mater. **22**, 4643–4648 (2010)
37. M. Gonzalez, F. Axisa, F. Bossuyt, Y.Y. Hsu, B. Vandevelde, J. Vanfleteren, Design and performance of metal conductors for stretchable electronic circuits. Circuit World **35**, 22–29 (2009)
38. G. Mani, M.D. Feldman, D. Patel, C.M. Agrawal, Coronary stents: a materials perspective. Biomaterials **28**, 1689–1710 (2007)
39. T. Widlund, S. Yang, Y.-Y. Hsu, N. Lu, Stretchability and compliance of freestanding serpentine-shaped ribbons. Int. J. Solids Struct. **51**, 4026–4037 (2014)
40. S. Yang, S. Qiao, N. Lu, Elasticity solutions to freestanding, non-buckling serpentine ribbons. To be submitted (2016)
41. D.H. Kim, R. Ghaffari, N.S. Lu, S.D. Wang, S.P. Lee, H. Keum et al., Electronic sensor and actuator webs for large-area complex geometry cardiac mapping and therapy. Proc. Natl. Acad. Sci. U.S.A. **109**, 19910–19915 (2012)
42. Y.L. Yu, D. Sanchez, N.S. Lu, Work of adhesion/separation between soft elastomers of different mixing ratios. J. Mater. Res. **30**, 2702–2712 (2015)

43. Y.W. Su, J. Wu, Z.C. Fan, K.C. Hwang, J.Z. Song, Y.G. Huang et al., Postbuckling analysis and its application to stretchable electronics. J. Mech. Phys. Solids **60**, 487–508 (2012)
44. Y.H. Zhang, S. Xu, H.R. Fu, J. Lee, J. Su, K.C. Hwang et al., Buckling in serpentine microstructures and applications in elastomer-supported ultra-stretchable electronics with high areal coverage. Soft Matter **9**, 8062–8070 (2013)
45. Y. Zhang, H. Fu, Y. Su, S. Xu, H. Cheng, J.A. Fan, et al., Mechanics of ultra-stretchable self-similar serpentine interconnects. Acta Mater. **61**, 7816–7827, (2013)
46. Y. Zhang, H. Fu, S. Xu, J.A. Fan, K.-C. Hwang, J. Jiang, et al., A hierarchical computational model for stretchable interconnects with fractal-inspired designs. J. Mech. Phys. Solids, **72**, 115–130 (2014)
47. Y.Y. Hsu, M. Gonzalez, F. Bossuyt, F. Axisa, J. Vanfleteren, I. DeWolf, The effect of pitch on deformation behavior and the stretching-induced failure of a polymer-encapsulated stretchable circuit. J. Micromech. Microeng. **20** (2010)
48. Y.Y. Hsu, M. Gonzalez, F. Bossuyt, F. Axisa, J. Vanfleteren, B. Vandevelde et al., Design and analysis of a novel fine pitch and highly stretchable interconnect. Microelectron. Int. **27**, 33–38 (2010)
49. M. Gonzalez, B. Vandevelde, W. Christiaens, Y.Y. Hsu, F. Iker, F. Bossuyt et al., Design and implementation of flexible and stretchable systems. Microelectron. Reliab. **51**, 1069–1076 (2011)
50. S. Yang, B. Su, G. Bitar, N. Lu, Stretchability of indium tin oxide (ITO) serpentine thin films supported by Kapton substrates. Int. J. Fract. **190**, 99–110, (2014)
51. S. Yang, E. Ng, N. Lu, Indium tin oxide (ito) serpentine ribbons on soft substrates stretched beyond 100%. Extreme Mech. Lett. **2**, 37–45 (2015)
52. U. Betz, M.K. Olsson, J. Marthy, M.F. Escola, F. Atamny, Thin films engineering of indium tin oxide: Large area flat panel displays application. Surf. Coat. Technol. **200**, 5751–5759 (2006)
53. H. Schmidt, H. Flugge, T. Winkler, T. Bulow, T. Riedl, W. Kowalsky, Efficient semitransparent inverted organic solar cells with indium tin oxide top electrode. Appl. Phys. Lett. **94** (2009)
54. Y. Leterrier, L. Medico, F. Demarco, J.A.E. Manson, U. Betz, M.F. Escola et al., Mechanical integrity of transparent conductive oxide films for flexible polymer-based displays. Thin Solid Films **460**, 156–166 (2004)
55. N.S. Lu, X. Wang, Z. Suo, J. Vlassak, Metal films on polymer substrates stretched beyond 50%. Appl. Phys. Lett. **91**, 221909 (2007)
56. R.M. Niu, G. Liu, C. Wang, G. Zhang, X.D. Ding, J. Sun, Thickness dependent critical strain in submicron Cu films adherent to polymer substrate. Appl. Phys. Lett. **90** (2007)
57. N.S. Lu, Z.G. Suo, J.J. Vlassak, The effect of film thickness on the failure strain of polymer-supported metal films. Acta Mater. **58**, 1679–1687 (2010)
58. S. Yang, Y.C. Chen, L. Nicolini, P. Pasupathy, J. Sacks, S. Becky et al., "Cut-and-paste" manufacture of multiparametric epidermal sensor systems. Adv. Mater. (2015). doi:10.1002/adma.201502386
59. M.D. Casper, A.Ö. Gözen, M.D. Dickey, J. Genzer, J.-P. Maria, Surface wrinkling by chemical modification of poly(dimethylsiloxane)-based networks during sputtering. Soft Matter **9**, 7797 (2013)
60. S. Choi, J. Park, W. Hyun, J. Kim, J. Kim, Y.B. Lee et al., Stretchable Heater Using Ligand-Exchanged Silver Nanowire Nanocomposite for Wearable Articular Thermotherapy. ACS Nano **9**, 6626–6633 (2015)
61. S. Hong, H. Lee, J. Lee, J. Kwon, S. Han, Y.D. Suh et al., Highly stretchable and transparent metal nanowire heater for wearable electronics applications. Adv. Mater. **27**, 4744–4751 (2015)
62. X. Huang, Y.H. Liu, K.L. Chen, W.J. Shin, C.J. Lu, G.W. Kong et al., Stretchable, wireless sensors and functional substrates for epidermal characterization of sweat. Small **10**, 3083–3090 (2014)

63. Z.Y. Huang, W. Hong, Z. Suo, Nonlinear analyses of wrinkles in a film bonded to a compliant substrate. J. Mech. Phys. Solids **53**, 2101–2118 (2005)
64. J. Xiao, A. Carlson, Z.J. Liu, Y. Huang, J.A. Rogers, Analytical and experimental studies of the mechanics of deformation in a solid with a wavy surface profile. J. Appl. Mech. **77**, 011003 (2009)
65. L. Wang, N. Lu, Conformability of a thin elastic membrane laminated on a soft substrate with slightly wavy surface. J. Appl. Mech. under review (2016)
66. S. Qiao, J.-B. Gratadour, L. Wang, N. Lu, Conformability of a thin elastic membrane laminated on a rigid substrate with corrugated surface
67. T.J. Wagner, D. Vella, The sensitivity of graphene "snap-through" to substrate geometry. Appl. Phys. Lett. **100**, 233111 (2012)
68. S. Scharfenberg, N. Mansukhani, C. Chialvo, R.L. Weaver, N. Mason, Observation of a snap-through instability in graphene. Appl. Phys. Lett. **100**, 021910 (2012)
69. N. Lu, D.H. Kim, Flexible and stretchable electronics paving the way for soft robotics. Soft Robotics **1**, 53–62 (2013)
70. M.A. Pacheco, C.L. Marshall, Review of dimethyl carbonate (DMC) manufacture and its characteristics as a fuel additive. Energy Fuels **11**, 2–29 (1997)